

# Solar coronal heating by magnetic cancellation – I. Connected equal bipoles

B. von Rekowski,<sup>\*</sup> C. E. Parnell and E. R. Priest

*School of Mathematics and Statistics, University of St Andrews, North Haugh, St Andrews KY16 9SS*

Accepted 2005 October 27. Received 2005 October 20; in original form 2005 August 17

## ABSTRACT

We present two-dimensional numerical magnetohydrodynamic simulations of a cancelling magnetic feature and the associated coronal X-ray bright point. Coronal reconnection is found to produce significant Ohmic heating, and at the same time about 90 per cent of the magnetic flux is cancelled. The presence of downflows accelerates the process of flux cancellation in the early phase. The last 10 per cent of the cancellation takes place by reconnection at the base. Reconnection occurs in a time-dependent way in response to the footpoint motions, and the resulting sequence of magnetic configurations is close to potential.

**Key words:** MHD – Sun: corona – Sun: magnetic fields.

## 1 INTRODUCTION

Observations have revealed that the normal solar coronal temperature varies between about 1 and 5 million kelvin. Large-scale coronal events, such as solar flares and coronal mass ejections (CMEs), cannot heat the whole corona because these events are not sufficiently widespread throughout the corona, they are too few in number, and thermal conduction across the magnetic field lines is effectively negligible. Moreover, the corona still maintains a temperature of over a million kelvin at solar minimum (quiet Sun), when there are usually weeks without any solar flares or CMEs.

Instead, it is likely that the many small-scale events in the quiet-Sun corona (such as bright points, microflares and nanoflares) provide almost all the heat (e.g. Parnell & Jupp 2000; Parnell & Galsgaard 2004; Mackay et al. 2000). This is plausible, given that the small-scale coronal magnetic field has a complex structure, with photospheric magnetic fragments of opposite polarity having multiple connections (e.g. Beveridge, Priest & Brown 2002; Close et al. 2004). These magnetic sources are in constant motion, and new flux is emerging frequently and old flux is cancelling. Consequently, this should lead to continual widespread magnetic reconnection and subsequent local heating throughout the whole corona, even when the Sun is quiet. Several two- and three-dimensional theoretical models have been developed over the past decade to study the reconnection processes in this context (e.g. Parnell, Priest & Golub 1994a; Parnell, Priest & Titov 1994b; Priest, Parnell & Martin 1994; Mandrini et al. 1996; Longcope 1998; Longcope & Kankelborg 1999; Longcope et al. 2001).

It has been found recently from observations that the flux recycling time (namely the time it takes to reconnect all the flux) is at most only 1.5 h in the quiet-Sun corona, which is around 1/10 of the photospheric flux recycling time (Close et al. 2004). One type of

observed small-scale heating phenomenon is coronal X-ray bright points (XBPs), which are spread over all latitudes and longitudes of the low quiet-Sun corona (Golub et al. 1974). Coronal BPs have been observed to release energies of the order of  $10^{27}$  to  $10^{28}$  erg. This is because typical energy release rates from BPs range between  $3 \times 10^{23}$  and  $10^{24}$  erg s<sup>-1</sup> (Habbal & Withbroe 1981), and the average lifetime of a BP is about 8 h (Golub et al. 1974), with lifetimes ranging between 2 and 48 h (Golub, Krieger & Vaiana 1976). In the following, we estimate that XBPs are likely to account for at least about 20 per cent of the heating of the quiet-Sun corona, assuming  $3 \times 10^{23}$  erg s<sup>-1</sup> for the heating rate and 2 h for the lifetime of an XBP (which yields about  $2 \times 10^{27}$  erg of released energy).

Withbroe & Noyes (1977) report an energy loss rate of  $3 \times 10^5$  erg cm<sup>-2</sup> s<sup>-1</sup> in the quiet-Sun corona. In order to maintain the temperature of the quiet-Sun corona, the energy losses need to be compensated by an energy input at the same rate. In order to find out the contribution to heating by XBPs, it is necessary to know the rate of occurrence of XBPs on the quiet Sun. XBPs can be caused by ephemeral regions (ERs: small-scale bipolar regions of emerging magnetic flux, located all over the solar surface) or by so-called cancelling magnetic features (CMFs: small-scale opposite-polarity regions of cancelling magnetic flux, also located all over the solar surface). Hagenaar (2001) estimates that the flux emerging in those ephemeral regions that are likely to create a BP is about  $5 \times 10^{23}$  Mx per day on the whole Sun, and finds that the absolute flux in an ER is  $10^{19}$  Mx on average. This agrees with observations of Golub et al. (1977), who find that the magnetic flux in a typical XBP above an ER (which naturally contains the flux of two ERs) is about  $2 \times 10^{19}$  Mx. As a result, there should be an average number of about  $5 \times 10^4$  ERs (with BP) emerging per day on the whole Sun. Assuming now that the energy of a BP from an ER is  $2 \times 10^{27}$  erg (see above), this yields an average energy release rate from BPs due to ERs of about  $10^{32}$  erg d<sup>-1</sup> on the whole Sun; that is, of about  $2 \times 10^4$  erg cm<sup>-2</sup> s<sup>-1</sup>. This is about 6.5 per cent of the required heating rate. Around two-thirds of XBPs, however, are located above sites

<sup>\*</sup>E-mail: brigitta@mcs.st-and.ac.uk

of CMFs (Harvey 1985, 1996; Webb et al. 1993). This suggests that there are about twice as many CMFs as ERs, counting only those with an associated XBP; that is, about  $10^5$  CMFs (with BP) per day on the whole Sun. The total flux loss rate through CMFs has to equal the total flux emergence rate through ERs, and thus it is  $5 \times 10^{23} \text{ Mx d}^{-1}$ . Therefore, a CMF contains on average  $5 \times 10^{18} \text{ Mx}$  absolute flux. Assuming that the energy of a BP from a CMF is  $2 \times 10^{27} \text{ erg}$ , too, then an average energy release rate from BPs due to CMFs is about  $4 \times 10^4 \text{ erg cm}^{-2} \text{ s}^{-1}$ , which is about 13 per cent of the required heating rate. Thus, an average total energy release rate from BPs (due to ERs and CMFs) is about  $6 \times 10^4 \text{ erg cm}^{-2} \text{ s}^{-1}$ , which is about 20 per cent of the required heating rate.

XBPs above CMFs are coronal brightenings that are caused by the interaction of photospheric magnetic fragments of different polarities, possibly involving more than one filament of each polarity, where the interaction involves the mutual loss of flux in equal proportions from each polarity. CMFs involve flux convergence (Livi, Wang & Martin 1985) and flux submergence (Harvey et al. 1999), and significant downflows can be present (Chae, Moon & Pevtsov 2004). Cancellation, reconnection and coronal heating through XBP formation are linked (e.g. Priest et al. 1994; Parnell et al. 1994a,b; Rickard & Priest 1994; Parnell & Priest 1995), and by studying them it should be possible to solve an important part of the coronal heating problem.

Priest et al. (1994) developed a theoretical model aimed at explaining bright points during CMFs. They start with a configuration with two equal photospheric magnetic line sources of opposite polarity (minus and plus) and an overlying coronal field, where the two line sources and the two flux systems associated with these poles are disconnected at and above the photosphere. As the opposite poles of the magnetic bipole are driven towards each other by a photospheric horizontal flow, the XBP event in the theoretical model passes through three phases: Priest et al. (1994) call these the pre-interaction phase, interaction phase and cancellation phase.

The pre-interaction phase is the phase during which the two poles remain unconnected as they approach each other; it occurs before an X-point is created. The interaction phase begins when the magnetic poles become sufficiently close to each other that a second-order null point forms between them in the photosphere. Assuming that the magnetic field evolves through a series of equipotential states as the poles are driven further towards each other, the null point rises into the corona, becoming an X-point, and drops back onto the photosphere during the interaction phase. Reconnection starts the moment the X-point forms, and continues throughout the interaction phase. The coronal reconnection around the X-point causes a bright point to appear and hot plasma to flow along the separatrices. To determine the maximum energy released during the interaction phase, it is assumed that no reconnection occurs and that a current sheet forms along the vertical line between the X-point and the corresponding point at the photosphere. The energy stored in the current sheet is found to be that observed in a BP. The cancellation phase starts once the X-point has dropped back onto the photosphere, so that cancellation happens entirely via photospheric reconnection. The main aim of Priest et al. (1994) was to explain XBPs arising from cancelling flux, and not to explain CMF events. Indeed, they do not model the cancellation phase in detail. As a result of their assumption of line sources, cancellation has to happen instantaneously, meaning that it can occur only at the end of the XBP event, and thus in the photosphere, after coronal reconnection has ceased.

What we find from our numerical experiments is basically that the interaction phase (coronal reconnection phase) and the cancellation

phase overlap in time. Our goal was to perform two-dimensional numerical magnetohydrodynamic (MHD) simulations in order to study the dynamics of the cancellation and reconnection processes in CMFs, together with the associated formation of coronal XBPs. We build on a previous numerical model developed by Rickard & Priest (1994), with the focus on modelling a complete CMF event and not a complete XBP event. Therefore, similar to in Rickard & Priest (1994), our MHD simulations start at a point where those bipolar sources that will be driven towards each other are partially connected in such a way that they are marginally touching at the base. It is essential for the study of the cancellation process that the sources are not line/point sources. The model involves four sources of alternating polarity, and an overlying field is created by flux connecting the two outer sources. Equal amounts of flux are connecting neighbouring inner and outer sources. Thus, the initial setup consists of four topologically distinct flux systems that are separated by two upper and two lower separatrices that intersect at a coronal X-point. With time, the two inner sources are pushed together by a driver at the base.

As a result of the fact that we do not model the phase from the unconnected state to our starting point, the calculated heat output is a lower limit. We do, however, model the whole cancellation phase, in contrast to Rickard & Priest (1994), who were able to run their experiment only for a very short time owing to numerical problems. (Because their maximum driving speed is 1/100 of our standard maximum driving speed, their simulation time of about 550 corresponds to a time period of about only 5.5 in our simulations.) The CMF event is completed when all vertical magnetic flux of the inner sources (the cancelling bipole) is cancelled.

In this paper, all bipolar sources considered have not only the same size, but also the same magnetic field magnitude and the same flux distribution, in order to facilitate comparison with Rickard & Priest (1994) and Priest et al. (1994), where appropriate. As an innovation, however, the simulated CMF evolves under the influence of different lower boundary conditions: these are (i) closed (i.e. no downflow), or (ii) allowing for downflows. We compute the dynamical magnetic field configurations during the modelled CMF event and compare them with the field configurations resulting from the theoretical model of Priest et al. (1994). Further, we determine the locations of current-sheet formation, the reconnection rates, dynamic flux structures and times of total cancellation. We calculate the energy output resulting from the reconnection event, and find that magnetic energy is efficiently converted to thermal energy as a result of Ohmic heating, yielding energy release rates at the lower limit of those observed in BPs. Thus, our MHD simulations support observational and theoretical suggestions that CMFs are elementary heating events of the quiet-Sun corona.

Our paper is structured as follows. In Section 2, we describe the model upon which our numerical experiments are based; the various experiments are then specified in Section 3. The results are presented in Section 4, and a summary and suggestions for future work are given in Section 5.

## 2 THE MODEL

### 2.1 Basic equations

We restrict ourselves to two spacial dimensions, using Cartesian coordinates  $(x, z)$ . We adopt the usual notation, where  $\mathbf{u}$  is the velocity field,  $\rho$  is the plasma density,  $p$  is the plasma pressure,  $\mathbf{A}$  is the magnetic vector potential,  $\mathbf{B} = \nabla \times \mathbf{A}$  is the magnetic field,  $\mathbf{J} = \nabla \times \mathbf{B}/\mu_0$  is the current density,  $\mu_0 = 4\pi$  is the magnetic permeability,

$\mathbf{E} = -\mathbf{u} \times \mathbf{B} + \eta \mu_0 \mathbf{J}$  is the electric field, and  $\eta$  is the magnetic diffusivity. In the two-dimensional system, we therefore have the two velocity components  $u_x, u_z$ , and the two magnetic field components  $B_x, B_z$ . The magnetic vector potential can be gauged such that it has only one component,  $A_y$ . We solve the induction equation in terms of the magnetic vector potential so that the condition  $\nabla \cdot \mathbf{B} = 0$  is fulfilled. Relevant quantities can be formulated in terms of  $A_y$  as

$$B_x = -\partial_z A_y, \quad B_z = \partial_x A_y, \quad J_y = -\Delta A_y / \mu_0,$$

$$\mathbf{J} \times \mathbf{B} = -\Delta A_y \nabla A_y / \mu_0,$$

$$(\mathbf{u} \times \mathbf{B})_y = -\mathbf{u} \cdot \nabla A_y = -E_y - \eta \Delta A_y,$$

$$\mathbf{E} \times \mathbf{B} / \mu_0 = (\mathbf{u} \cdot \nabla A_y) \nabla A_y / \mu_0 + \eta \Delta A_y \nabla A_y / \mu_0.$$

Owing to the fact that we model just a part of the corona, a reasonable first assumption is that the medium be isothermal so that  $p = c_s^2 \rho$ , with the isothermal sound speed  $c_s$  being constant. For simplicity, we neglect gravity.

Under these assumptions, we solve the time-dependent MHD equations, namely the continuity equation,

$$\frac{\partial \ln \rho}{\partial t} + \mathbf{u} \cdot \nabla \ln \rho = -\nabla \cdot \mathbf{u}, \quad (1)$$

the Navier–Stokes equation,

$$\frac{\partial \mathbf{u}}{\partial t} + (\mathbf{u} \cdot \nabla) \mathbf{u} = -c_s^2 \nabla \ln \rho - \frac{1}{\mu_0 \rho} \Delta A_y \nabla A_y + \nu \nabla \cdot \boldsymbol{\sigma} + \nu \boldsymbol{\sigma} \cdot \nabla \ln(\rho \nu), \quad (2)$$

and the uncurred induction equation,

$$\frac{\partial A_y}{\partial t} + \mathbf{u} \cdot \nabla A_y = \eta \Delta A_y. \quad (3)$$

Here,  $\rho \nu \boldsymbol{\sigma}$  is the viscous stress tensor with the components  $\rho \nu \sigma_{ij} \equiv \rho \nu (\partial u_i / \partial x_j + \partial u_j / \partial x_i)$ ,  $\nu$  is the kinematic viscosity, and  $t$  is time.

## 2.2 Normalization and model parameters

Our normalization parameters are typical values for the length-scale,  $l_0$ , the magnetic field strength,  $B_0$ , and the plasma density,  $\rho_0$ , of the considered system in the quiet-Sun corona.

A photospheric source is typically between about 5 and 10 Mm in diameter, so we choose  $l_0 = 5$  Mm as our length unit. However, the base of our system is located in the low corona, above the photosphere, where the sources have expanded from their photospheric concentrations. Therefore, we choose for our sources a width of  $d_{\text{src}} = l_{\text{src}} l_0$  with  $l_{\text{src}} = 3$ , so that  $d_{\text{src}} = 15$  Mm. A characteristic magnetic field strength in the low quiet-Sun corona is of the order of a few gauss. We choose  $B_0 = 5$  G as our field strength unit, and start with a magnetic field configuration in which the maximum field strength of each source at our base is  $B_{\text{src}} = (1/\alpha_{\text{src}}) B_0$  (see Section 2.3). By choosing  $\alpha_{\text{src}} = 0.353$ , we have  $B_{\text{src}} \approx 2.83 B_0 \approx 14$  G. Finally, we choose a characteristic plasma density of  $\rho_0 = 10^{-16}$  g cm $^{-3}$  as our density unit, which is also our initial density.

Having chosen these three normalization parameters, the physical units of all the quantities used in the system are fixed. The resulting velocity unit is  $v_0 \equiv B_0 / \sqrt{4\pi \rho_0} \approx 1400$  km s $^{-1}$ , which is a typical Alfvén speed in the low corona. In our initial setup, the Alfvén speed at the base is equal to  $v_0$  around  $x = l_{\text{src}}$  and  $x = 3 l_{\text{src}}$ . Throughout the runs of our numerical experiments,  $v_0$  remains a characteristic Alfvén speed at the base. The time unit is  $t_0 \equiv l_0 / v_0 \approx 3.6$  s (so that 1000 dimensionless time units correspond to 1 h), the unit for

the magnetic diffusivity and kinematic viscosity is  $\eta_0 \equiv l_0 v_0 \approx 7 \times 10^{16}$  cm $^2$  s $^{-1}$ , the energy unit is  $W_0 \equiv B_0^2 l_0^3 / (4\pi) \approx 2.5 \times 10^{26}$  G $^2$  cm $^3 = 2.5 \times 10^{26}$  erg, and the unit for the magnetic flux is  $F_0 \equiv B_0 l_0^2 = 1.25 \times 10^{18}$  G cm $^2 = 1.25 \times 10^{18}$  Mx. With this normalization, the only change to the above equations and quantities is to drop  $\mu_0$  in their dimensionless form.

Our model parameter for the thermodynamics is the isothermal coronal sound speed, which we choose to be one-tenth of the characteristic Alfvén speed  $v_0$ ; that is,  $c_s = 0.1 v_0 \approx 140$  km s $^{-1}$ . Because  $T = c_s^2 \mu / \mathcal{R}$  for an isothermal perfect gas (where  $\mathcal{R} \approx 8.3 \times 10^7$  cm $^2$  s $^{-2}$  K $^{-1}$  is the gas constant and  $\mu = 0.6$  is the mean specific weight), our isothermal coronal temperature is  $T = 0.01 v_0^2 \mu / \mathcal{R} \approx 1.4 \times 10^6$  K.

## 2.3 Initial setup

We shall use dimensionless quantities unless stated otherwise. Similar to in Rickard & Priest (1994), we start with an initial magnetic field configuration with four magnetic sources of alternating polarity at the lower boundary of our computational domain, as depicted in Fig. 1. The lower boundary ( $z = 0$ ) is located somewhat above the photosphere, in the low corona, and we consider a coronal region of height  $2 l_{\text{src}}$  ( $0 \leq z \leq 2 l_{\text{src}}$ ) and width  $4 l_{\text{src}}$  ( $0 \leq x \leq 4 l_{\text{src}}$ ). This is effectively an area of  $60 \times 30$  Mm $^2$ . We assume that all four sources at  $z = 0$  are equal, apart from their polarity. This implies that they are equal in size, strength and flux distribution. The top, left and right boundaries of our computational domain are closed. By making a potential field extrapolation from the boundaries, we obtain the uniquely determined minimum energy magnetic field in the domain as our initial field. Neighbouring sources are connected to each other, as well as to the two outer sources, the latter connection forming an overlying field. Therefore, the initial magnetic field configuration is composed of four different flux systems, which are symmetric about the middle vertical axis,  $x = 2 l_{\text{src}} = 6$  (which we will just call the axis). The flux systems are separated by two upper and two lower separatrices that intersect at an X-point, which is located on the axis, initially at a height  $z = 1.88$ .

Our initial magnetic field is potential, except at the lower boundary ( $z = 0$ ). In line with Rickard & Priest (1994), we model the four sources by setting

$$A_y(x, 0) = \begin{cases} \tanh\left(\frac{x-1/2 l_{\text{src}}}{\alpha_{\text{src}}}\right), & x \in [0, l_{\text{src}}] \\ \tanh\left(\frac{-x+3/2 l_{\text{src}}}{\alpha_{\text{src}}}\right), & x \in [l_{\text{src}}, 2 l_{\text{src}}] \\ \tanh\left(\frac{x-5/2 l_{\text{src}}}{\alpha_{\text{src}}}\right), & x \in [2 l_{\text{src}}, 3 l_{\text{src}}] \\ \tanh\left(\frac{-x+7/2 l_{\text{src}}}{\alpha_{\text{src}}}\right), & x \in [3 l_{\text{src}}, 4 l_{\text{src}}] \end{cases}. \quad (4)$$

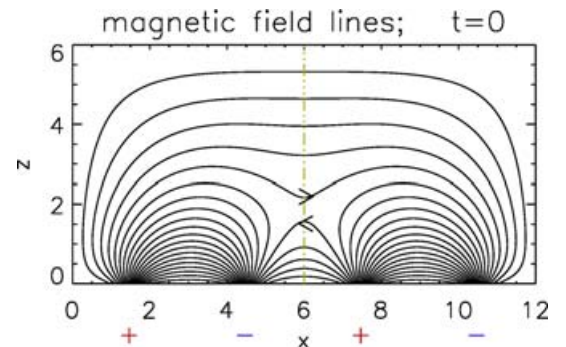


Figure 1. Initial magnetic field lines (at time  $t = 0$ ).

Hence, with  $l_{\text{src}}$  being the width of each source, all four sources are equal except that they have alternating polarity: the first one is positive ( $B_z > 0$ , polarity  $s_1 = +1$ ), the second one is negative ( $B_z < 0$ , polarity  $s_2 = -1$ ), the third one is positive ( $s_3 = +1$ ), and the fourth one is negative ( $s_4 = -1$ ). The vertical magnetic field component of the four sources ( $i = 1, \dots, 4$ ;  $x \in [(i-1)l_{\text{src}}, i l_{\text{src}}]$ ) is

$$B_z^i(x, 0) = \frac{s_i}{\alpha_{\text{src}}} \left( 1 - \tanh^2 \left( \frac{x - (i-1/2)l_{\text{src}}}{\alpha_{\text{src}}} \right) \right), \quad (5)$$

so as already discussed it is clear that  $1/\alpha_{\text{src}}$  is the maximum magnetic field strength of each source [reached at  $x = (i-1/2)l_{\text{src}}$ ], and  $B_z^i$  vanishes at the source edges. The normalized magnetic flux per unit length in each of our sources is

$$\begin{aligned} \int_{(i-1)l_{\text{src}}}^{i l_{\text{src}}} B_z^i(x, 0) dx &= A_y(x, 0) \Big|_{(i-1)l_{\text{src}}}^{i l_{\text{src}}} \\ &= 2s_i \tanh \left( \frac{l_{\text{src}}}{2\alpha_{\text{src}}} \right) \approx 2s_i, \end{aligned} \quad (6)$$

corresponding to  $\vec{F}_{\text{src}} \approx 2s_i (F_0/l_0) = \pm 5 \times 10^9 \text{ Mx cm}^{-1}$ . If the flux were distributed in the missing  $y$ -direction with the same profile as in the  $x$ -direction, this would result in an unsigned flux of  $F_{\text{src}} \approx 2l_{\text{src}} F_0 = 7.5 \times 10^{18} \text{ Mx}$  in each source, which would be a strong CMF. The total flux in the considered XBP is twice as much as that in the CMF; that is, it would be about  $1.5 \times 10^{19} \text{ Mx}$ . The maximum strength of our overlying field is initially about 1 G, and at most doubles in magnitude during the experiments.

The top, left and right boundaries of our computational domain are closed, so respectively we obtain

$$A_y(x, 2l_{\text{src}}) = A_y(0, 0), \quad x \in [0, 4l_{\text{src}}], \quad (7)$$

$$A_y(0, z) = A_y(0, 0), \quad z \in [0, 2l_{\text{src}}], \quad (8)$$

$$A_y(4l_{\text{src}}, z) = A_y(0, 0), \quad z \in [0, 2l_{\text{src}}]. \quad (9)$$

The initial magnetic field in the whole domain is mirror-antisymmetric with respect to the axis; that is,  $B_x$  is symmetric and  $B_z$  is antisymmetric.

The initial potential magnetic field – depicted in Fig. 1 – is then obtained by solving the Laplace equation for the magnetic vector potential,

$$\Delta A_y = 0, \quad (10)$$

by simple Jacobi iteration, which converges to machine accuracy (in double precision) in about 55 000 iteration steps. (The simple Jacobi iteration used involves one neighbouring point – in each of the four directions – to the respective point at which the Laplace operator is calculated.)

There is no initial velocity field in the domain, and the initial dimensionless density is 1 everywhere in the domain.

## 2.4 Boundary conditions and the numerical code

In all our numerical simulations we have a uniformly spaced mesh, with 199 grid points in  $x$  and 100 grid points in  $z$ , so that the mesh sizes are  $\delta x = \delta z \approx 0.06$ .

For the density, we make an extrapolation to the boundaries that corresponds to

$$\frac{\partial^2 \rho}{\partial n^2} = 0 \quad (11)$$

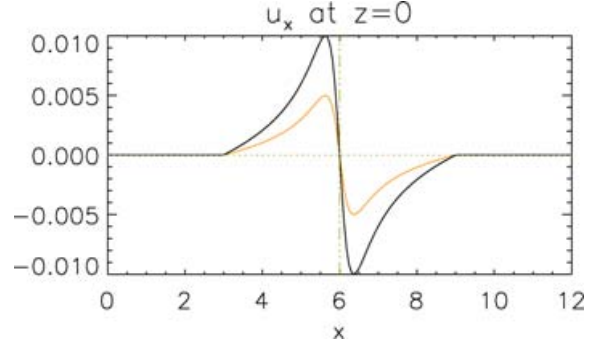


**Figure 2.** Horizontal velocity driver at the base. Two different maximum speeds are chosen:  $u_{\text{driver}} = 0.01$  (black curve) and  $u_{\text{driver}} = 0.005$  (orange/grey curve).

at the first point into the domain. Here,  $n$  is the direction normal to the respective boundary, and we use the second-order centred finite-difference scheme for calculating the second derivatives. In order to avoid unphysical behaviour of the density at the base-point of the axis ( $x = 2l_{\text{src}}$  and  $z = 0$ ), we ensure that the density at the bottom boundary neither drops below nor exceeds the threshold limits of 0.2 and 5, respectively. This is necessary to compensate for the neglect of gravity in our experiments.

We consider a system that remains closed at the left, top and right boundaries, meaning a vanishing velocity at these edges. This is done in order to keep the initial magnetic field line that goes along these boundaries (and which forms the outermost line of the overlying field connecting the outer sources).

During our numerical simulations, the two outer sources are fixed at all times, whereas the two inner sources are moved towards each other by a horizontal velocity driver at the base, according to Fig. 2. Thus,

$$u_x(x, 0) = 0, \quad x \in [0, l_{\text{src}}] \cup [3l_{\text{src}}, 4l_{\text{src}}], \quad (12)$$

whereas the velocity driver is imposed as

$$u_x(x, 0) = u_{\text{driver}} \frac{u_{\text{prof}}(x)}{\max |u_{\text{prof}}(x)|}, \quad x \in [l_{\text{src}}, 2l_{\text{src}}], \quad (13)$$

with the maximum driving speed  $u_{\text{driver}}$ , and the profile of the driver

$$u_{\text{prof}}(x) = (2l_{\text{src}} - x) \left( \frac{1}{d_1} - \frac{1}{d_2} \right), \quad (14)$$

where  $d_1 = 1 + g_{\text{slope}} (2l_{\text{src}} - x)^2$  and  $d_2 = 1 + g_{\text{slope}} l_{\text{src}}^2$ . The parameter  $g_{\text{slope}}$  controls the steepness of the profile of the driver around the axis. We have chosen a rather high value of  $g_{\text{slope}} = 7$  to ensure a reasonable, not too low, driving speed around the axis, where the two inner sources will start to interact. The velocity driver is antisymmetric with respect to the axis  $x = 2l_{\text{src}}$ , so

$$u_x(x, 0) = -u_x(4l_{\text{src}} - x, 0), \quad x \in [2l_{\text{src}}, 3l_{\text{src}}]. \quad (15)$$

We drive the system at two different maximum speeds,  $u_{\text{driver}} = 0.01$  and  $u_{\text{driver}} = 0.005$ , corresponding to about 14 and 7  $\text{km s}^{-1}$ , respectively. These values are about 0.0035 (0.00175) times the initial *maximum* Alfvén speed, respectively, which is  $2.83 v_0 \approx 4000 \text{ km s}^{-1}$  and located at the base.

Regarding the vertical velocity, we consider two cases: case (i) with no downflow (experiments *NoDF* and *NoDF1/2*), and case (ii) with downflow (experiments *DF* and *DF1/2*); see Table 1. We will describe these two different cases of boundary conditions in Section 3.

The magnetic field at the base is determined through  $A_y$ , which is advected in time; that is, at the base we solve the induction equation (3) with zero  $\eta$ . Here, we use a second-order finite-difference scheme for calculating the first derivatives. Note that at the base it is important to solve the advection equation separately for the left and right halves. Computing the  $x$ -derivative with a finite-difference scheme that uses points on both sides causes problems during advection in  $x$  when the two inner sources are relatively close. We further set the conditions  $\partial^2 A_y / \partial x^2|_{z=0} = 0$  (i.e.  $\partial B_z / \partial x|_{z=0} = 0$ ) at the left and right neighbouring points of the axis, as well as  $\partial A_y / \partial x|_{z=0} = 0$  (i.e.  $B_z|_{z=0} = 0$ ) at the axis, both single sided and low order. These are natural conditions and stabilize the code.

In the domain excluding the boundaries, we use a sixth-order finite-difference scheme in space. The time advance method we use is always third-order Runge–Kutta.

### 3 NUMERICAL EXPERIMENTS

Our aim is to model a CMF event resulting from converging, submerging flux, and the associated XBP formation caused by coronal reconnection and Ohmic heating, in the presence of an overlying field. We carried out four dynamical numerical experiments, as listed in Table 1, and we computed the potential magnetic field at various times for comparison with the no-downflow experiments (*NoDF* and *NoDF1/2*). The four dynamical numerical experiments differ from each other in their treatment of the vertical velocity at the base, and in the speed of the horizontal driver (also located at the base), where  $u_{\text{driver}}$  is given in units of the characteristic Alfvén speed  $v_0$ .

In the numerical experiments *NoDF* and *NoDF1/2* we close the lower boundary to vertical flow; in particular, we prohibit any downflow, whilst in *DF* and *DF1/2* we allow for a downflow. This downflow is not imposed in shape or amplitude: we extrapolate the vertical flow from the domain onto the base by setting  $u_z(x, 0) = 2u_z(x, \partial z) - u_z(x, 2\partial z)$ . However, the downflow is restricted to the region between the moving magnetic strength maxima of the inner sources (we will call this the downflow region). This restriction of the downflow is important for two reasons. First, in this way we avoid a stagnation point, which otherwise would develop at some point and then prevent any further cancellation. Secondly, restricting the downflow to a region that becomes narrower and narrower with time means that the downflow will eventually cease, which turns out to be necessary for achieving complete cancellation. Upflows are not allowed in the downflow region, and outside the downflow region  $u_z$  is set to zero. The reason for this choice of boundary condition for the vertical flow at the base is to allow for a downflow that can develop as freely as possible, but that at the same time permits full cancellation. The whole flow, comprising the developing downflow in *DF* and *DF1/2*, is then included in the advection process of the inner sources at the lower boundary (see Section 2.4).

**Table 1.** Various model parameters of the numerical experiments discussed in this paper. The asterisk means that this table entry is explained in the text in Section 3. For comparison with experiments *NoDF* and *NoDF1/2*, we computed the potential magnetic field at various times (*Pot*).

Experiment	Description	$u_z^{z=0}$	$u_{\text{driver}}$
<i>NoDF</i>	No DownFlow	0	0.01
<i>DF</i>	DownFlow	$\leq 0^*$	0.01
<i>NoDF1/2</i>	No DownFlow; 1/2 speed	0	0.005
<i>DF1/2</i>	DownFlow; 1/2 speed	$\leq 0^*$	0.005
<i>Pot</i>	Potential field	0	–

In the domain except the base, the magnetic diffusivity is proportional to the magnitude of the current density (with proportionality constant equal to 1, so that during the runs the maximum  $\eta$  is about 0.08 in *DF* and 0.12 in *NoDF*), but  $\eta$  is not allowed to be smaller than 0.005. This leads to an enhanced magnetic diffusivity in the region of strong currents, but  $\eta$  remains close to the minimum value in the bulk of the domain. In all our numerical experiments we take  $\nu = 0.05$  for the kinematic viscosity.

## 4 RESULTS

### 4.1 Magnetic field configuration

In this section, we look at the time evolution of the magnetic field configuration during our complete CMF event. For various times, we plot in Figs 3 and 4 the magnetic field lines in the region that includes the two inner sources (in  $x$ ) and extends in  $z$  to half the height of the domain. Fig. 3 is for experiment *NoDF* (no downflow), whilst Fig. 4 is for experiment *DF* (downflow allowed). We compare the results of our numerical MHD simulations with the theoretical results of Priest et al. (1994). A comparison with the numerical results of Rickard & Priest (1994) is possible only for the very early phase of the CMF event, because their simulation spans only a very short time, and is briefly made in Section 4.4.

As already mentioned, we start with a configuration in which the X-point lies above our base, at a height of about 1.88, so that the sources of the inner bipole are connected; an overlying field is created by the connected outer sources [ $t = 0$ , panel (a) of

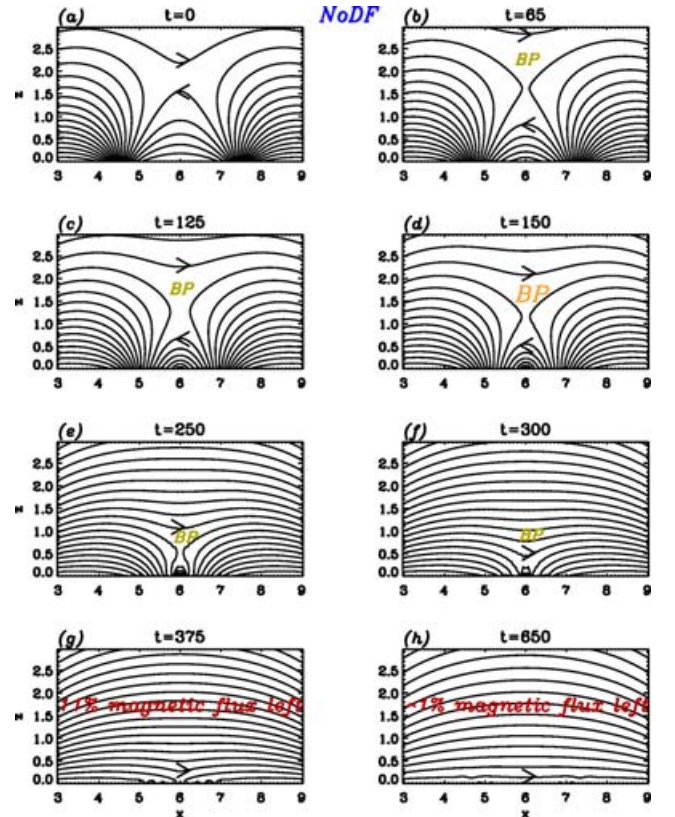


**Figure 3.** Magnetic field lines in experiment *NoDF* at various times. The region shown includes the two inner sources (in  $x$ ) and extends in  $z$  to half the height of the domain. ‘BP’ stands for ‘Bright Point’, i.e. significant Ohmic heating. Large (orange/grey) letters are at roughly the times of peak heating.

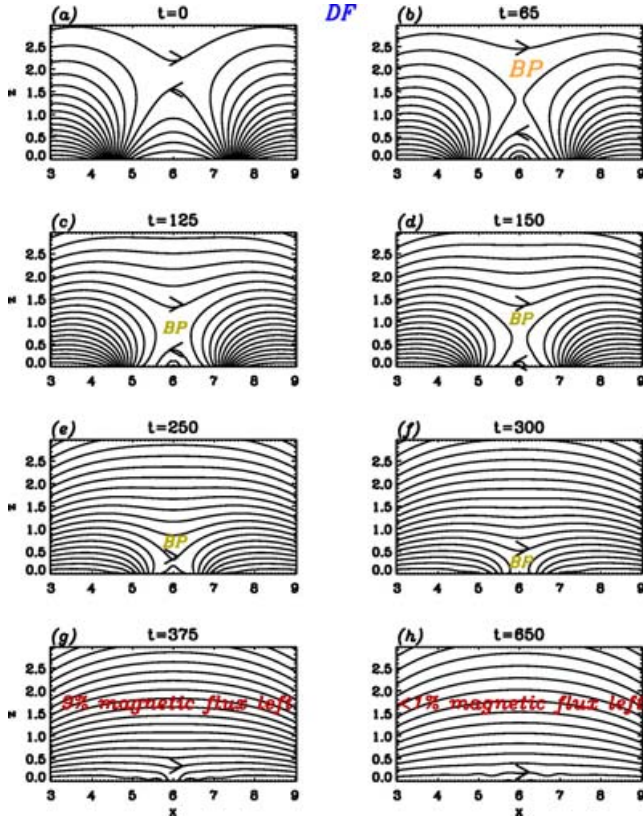


**Figure 4.** As Fig. 3, but for experiment *DF*.

Figs 3 and 4]. As the inner sources approach each other, unconnected field lines of the two inner sources reconnect around the X-point. (Here, ‘unconnected field lines’ actually refers to the field lines that connect the inner and outer sources on each side of the axis.) This coronal magnetic reconnection causes energy release in the form of heat due to Ohmic heating, consistent with Priest et al. (1994). In panels (b) to (f) of Figs 3 and 4, we write ‘BP’ in large (orange/grey) letters at roughly the times when the Ohmic heating peaks, whereas ‘BP’ is written in small (green/grey) letters at times when Ohmic heating is greater than approximately 10 per cent of the peak heating (see Section 4.2 for full details on the energetics).

As expected, coronal magnetic reconnection driven by converging sources implies that, with time, the X-point drops in height. When the X-point reaches the base, most opposite-polarity flux from the inner sources has already cancelled. This means that, whereas in the original theoretical model of Priest et al. (1994) flux cancellation is only at the photosphere and follows coronal reconnection, in our numerical experiments coronal reconnection and flux cancellation occur mostly simultaneously. When the X-point has reached the base, only about 10 per cent of the magnetic flux of the cancelling bipole is left [ $t = 375$ , panel (g) of Figs 3 and 4]. However, now it takes roughly the same time again to cancel almost all the remaining flux such that at most 1 per cent is left [ $t = 650$ , panel (h) of Figs 3 and 4]. This remaining flux cancellation happens by reconnection at the base.

Obvious differences between the experiments *NoDF* and *DF* are the time-scales at which coronal reconnection occurs, and the way magnetic flux ([re-]connecting the inner sources) is cancelled during the XBP phase. Before we analyse and compare how the reconnection and cancellation processes take place in the no-downflow and

downflow experiments (in Section 4.3), we look at the time evolution of the energetics.

## 4.2 Energetics

In Fig. 5 we plot various quantities as functions of time: the height of the X-point, the Poynting flux across the base, the magnetic and kinetic energies, the reconnection rate, and the Ohmic heating in the whole domain, as well as at the axis. The last panel of Fig. 5 is the legend for the various curves: black solid curves are for experiment *DF*, black dashed curves are for *DF1/2*, red/grey solid curves are for *NoDF*, red/grey dashed curves are for *NoDF1/2*, and the (blue) squares are for *Pot*. To begin with, we give the definitions of the non-normalized quantities and the physical units of the plotted dimensionless quantities (where  $\mu_0$  has dropped out); we will describe the results while discussing the effects of a downflow when comparing the no-downflow and downflow experiments in Section 4.3.

The X-point is located on the axis; its height is determined as the height at which  $B_x$  changes sign. The X-point height is given in units of  $l_0$  ( $= 5$  Mm) in Fig. 5, top left panel.

The Poynting flux across the base  $z = 0$  is the rate per unit length at which energy is removed from the system (if negative), or at which energy is injected into the system (if positive). (The top, left and right boundaries of our system are closed to normal flow, as well as to normal magnetic field, so there is no Poynting flux across those boundaries.) Because the driving at the base involves zero  $\eta$ , the Poynting flux across the bottom boundary is

$$\begin{aligned} P_{z=0} &= \frac{1}{\mu_0} \int_0^{4l_{\text{src}}} (\mathbf{E} \times \mathbf{B})_z \, dx \Big|_{z=0} \\ &= \frac{1}{\mu_0} \int_0^{4l_{\text{src}}} (-u_x B_x B_z + u_z B_x^2) \, dx \Big|_{z=0}, \end{aligned} \quad (16)$$

which we plot in units of  $W_0/(l_0 t_0) \approx 1.5 \times 10^{17} \text{ erg cm}^{-1} \text{ s}^{-1}$  in the top middle-left panel of Fig. 5.

The magnetic and kinetic energies are

$$E_{\text{mag}} = \int_0^{2l_{\text{src}}} \int_0^{4l_{\text{src}}} \frac{B^2}{2\mu_0} \, dx \, dz, \quad (17)$$

and

$$E_{\text{kin}} = \int_0^{2l_{\text{src}}} \int_0^{4l_{\text{src}}} \frac{\rho u^2}{2} \, dx \, dz, \quad (18)$$

respectively, which we plot in units of  $W_0/l_0 \approx 5 \times 10^{17} \text{ erg cm}^{-1}$  in the top middle-right and top right panels, respectively, of Fig. 5. It can be seen that the maximum kinetic energy is at least 4000 times smaller than the magnetic energy.

The reconnection rate is the rate at which magnetic flux is reconnected. All the flux reconnected crosses the axis and lies beneath the X-point. Therefore, the reconnection rate is

$$R_{\text{reco}} = \frac{\partial}{\partial t} \int_0^{h_{\text{xp}}} A_y \Big|_{x=6} \, dz = - \int_0^{h_{\text{xp}}} E_y \Big|_{x=6} \, dz \quad (19)$$

(Fig. 5, bottom left panel), where the height of the X-point,  $h_{\text{xp}}$ , drops with time; cf. the top left panel of Fig. 5.  $R_{\text{reco}}$  is in units of  $F_0/t_0 \approx 3.5 \times 10^{17} \text{ Mx s}^{-1}$ . The values in the bottom left panel of Fig. 5 are the total reconnected flux in the simulated event, given in units of  $F_0 = 1.25 \times 10^{18} \text{ Mx}$  for each of the dynamical numerical experiments. They are obtained by integrating the reconnection-rate curves over the time of the simulated event. As can be seen from these values, the total reconnected flux during a cancellation

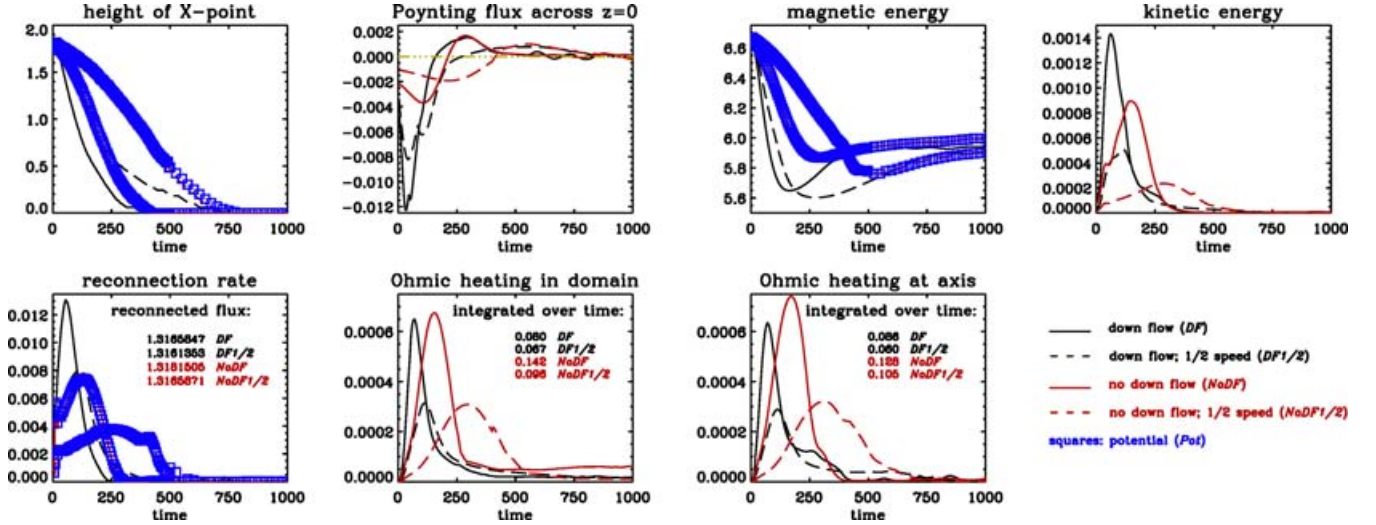


**Figure 5.** Various quantities as functions of time, illustrating the time evolution of the energetics. The bottom right panel is the legend for the various curves. The values in the other bottom panels are described in Section 4.2. (We do not plot the quantities at  $t = 0$ .)

event such as the one that we have studied is independent of the driving speed, as well as independent of transient downflows and the evolution of the magnetic field; this is because the initial states are the same and the final states are the same, too, in all our experiments discussed here. (The maximum variation in the values of the total reconnected flux of less than 1 per cent is the result of numerical errors.)

The values of Ohmic heating in the domain and at the axis are

$$O_{\text{heat}}^{\text{dom}} = \int_0^{2l_{\text{src}}} \int_0^{4l_{\text{src}}} \eta \mu_0 J^2 dx dz, \quad (20)$$

and

$$O_{\text{heat}}^{\text{axis}} = \int_0^{2l_{\text{src}}} \eta \mu_0 J^2 dz \Big|_{x=6}, \quad (21)$$

respectively, and we have plotted them in the bottom middle panels of Fig. 5. Ohmic heating is an energy rate; it is per unit length in our domain, and per unit length squared at the axis. We give these quantities in units of  $W_0/(l_0 t_0) \approx 1.5 \times 10^{17} \text{ erg cm}^{-1} \text{ s}^{-1}$  and  $W_0/(l_0^2 t_0) \approx 3 \times 10^8 \text{ erg cm}^{-2} \text{ s}^{-1}$ , respectively. We recall that our experiments start when the inner bipolar sources are partially connected, which means that the experiments do not cover a complete XBP event, although they do cover a complete cancellation event. Therefore, the values in the two bottom middle panels of Fig. 5 are lower limits to the total heat produced by an XBP, assuming that thermal energy release is entirely the result of Ohmic heating. These values are obtained by integrating the Ohmic heating curves over the time of the simulated event, and therefore they are in units of  $W_0/l_0 \approx 5 \times 10^{17} \text{ erg cm}^{-1}$  and  $W_0/l_0^2 \approx 10^9 \text{ erg cm}^{-2}$ , respectively.

In order to be able to compare the released energy in our experiments with observations of XBPs, we assume that heating in the three-dimensional domain occurs like heating in the two-dimensional domain, so we take the heat output in our two-dimensional domain and multiply by the width of the two inner sources,  $2l_{\text{src}}$ . The resulting released heat is  $\sim 6 \times 0.08$  in experiment *DF*,  $\sim 6 \times 0.142$  in *NoDF*,  $\sim 6 \times 0.067$  in *DF1/2*, and  $\sim 6 \times 0.096$  in *NoDF1/2* (in units of  $W_0 \approx 2.5 \times 10^{26} \text{ erg}$ ); that is, about  $(1 \dots 2) \times 10^{26} \text{ erg}$ . This is lower by about an order of magnitude than minimum released energies from BPs deduced from observations (see Section 1). Our BPs are, however, shorter-lived: they

have a lifetime of about 30 to 45 min (500 to 750 dimensionless time units), whereas the minimum BP lifetime observed by Golub et al. (1976) is 2 h. Therefore, it is better to compare heating rates. If we take the *maximum* heating rate in our domain, which is about 0.00065 [in units of  $W_0/(l_0 t_0)$ ], and multiply by the width of the two inner sources,  $2l_{\text{src}}$  (in units of  $l_0$ ), this gives a *maximum* heating rate of approximately  $2.7 \times 10^{23} \text{ erg s}^{-1}$ . This compares well with the *minimum* typical heating rate observed by Habbal & Withbroe (1981), which is  $3 \times 10^{23} \text{ erg s}^{-1}$ .

The *maximum* heating rates at the axis, about 0.00065 in *DF* and 0.00075 in *NoDF*, correspond to about  $2 \times 10^5 \text{ erg cm}^{-2} \text{ s}^{-1}$ , which is almost what is required to heat and maintain the temperature of the quiet-Sun corona: Withbroe & Noyes (1977) report an energy loss rate of  $3 \times 10^5 \text{ erg cm}^{-2} \text{ s}^{-1}$ . However, the *maximum* heating rates found in the two-dimensional domain would provide on average – when reduced to a one-dimensional slab – about  $4l_{\text{src}}$  ( $= 12$ ) times less heating, i.e. about  $1.5 \times 10^4 \text{ erg cm}^{-2} \text{ s}^{-1}$ , which is about 5 per cent of the required heating rate. This estimate assumes that only one BP occurs in our domain at a time.

We computed the potential field at various times for the case in which the magnetic flux at the base is advected with no downflow (*Pot*) for comparison with the dynamical evolution of the magnetic field in experiments *NoDF* and *NoDF1/2*. As can be seen in Fig. 5, the time evolutions of magnetic energy, height of the X-point and reconnection rate in *NoDF* and *NoDF1/2* are very similar to their time evolutions in the corresponding potential field runs. Virtually no free magnetic energy is created; in other words, magnetic energy conversion to heat is very efficient.

### 4.3 Comparison of the no-downflow and downflow experiments

Comparing the magnetic field structure of the experiments *NoDF* (Fig. 3) and *DF* (Fig. 4), it is obvious that, as the inner sources are driven towards each other in the early phase, the field lines connecting the inner sources are more strongly compressed in the no-downflow case (panels b to f of Fig. 3) than they are in the downflow case (panels b to f of Fig. 4). The comparison demonstrates that, in the early phase, the downflow increases the removal of magnetic flux, which is otherwise the result of cancellation associated with

reconnection. Reconnection occurs earlier and runs faster in the presence of a downflow: the maximum reconnection rate is at  $t \approx 60$  in *DF*, and at  $t \approx 125$  in *NoDF* (cf. Fig. 5, bottom left panel). This leads to a quicker drop off in magnetic energy for *DF* and *DF1/2* than for *NoDF* and *NoDF1/2*, respectively (cf. Fig. 5, top middle-right panel). As a consequence, the XBP (peak Ohmic heating) occurs earlier with downflow: maximum Ohmic heating is at  $t \approx 65$ , compared with  $t \approx 150$  without downflow (cf. Fig. 5, bottom middle panels). However, the quicker reconnection in the downflow case leads to a somewhat weaker and shorter-lived XBP. This is because the limited compression of the field by the downflow means that the build-up of currents is limited, and thus less energy is released. Naturally, the quicker the reconnection is, the faster the X-point drops (cf. Fig. 5, top left panel).

The more rapid flux removal in the presence of downflows also affects the early-phase time evolution of the kinetic energy in the domain and the evolution of the (at this stage negative) Poynting flux across the base; both peak earlier in the downflow case than in the case of no downflows (cf. Fig. 5, top right and top middle-left panels). In both cases, the Poynting flux has its minimum slightly before the reconnection rate has its maximum. The initially negative Poynting flux means that, at first, energy is removed from the system, reflecting the fact that, to begin with, driving the sources together is easy. In the no-downflow experiments, the reason that the Poynting flux becomes increasingly negative in the early phase is the above-mentioned flux compression, which leads to a greater contribution of the  $B_x$  component (which is negative) between the strength maxima of the inner sources. Hence, there is a larger contribution of  $-u_x B_x B_z$  (which is also negative) between the strength maxima of the inner sources, and hence a more negative Poynting flux in the no-downflow case. In the downflow experiments, the downflow ( $u_z < 0$ ) leads to an additional term in the Poynting flux, namely  $u_z B_x^2$ , which is less than zero in the downflow region. Because  $|u_z| > |u_x|$ , this additional term leads to an even greater negative peak in the Poynting flux in the downflow case: it is more pronounced and occurs earlier in time. This also means, however, that the negative peak in the Poynting flux is narrower in time in the downflow case.

The peak in the reconnection rate shows a similar behaviour, at a slightly later time. Thus, the reconnection-rate peak in a downflow experiment is higher in amplitude but narrower in time than in the corresponding no-downflow experiment. The reason is that the total reconnected flux has to be the same in all our experiments, because the initial states are the same, as are all the final states. Reconnection gives rise to enhanced plasma flow (see Figs 6 to 9), which explains the similar behaviour of the peaks in the kinetic energy and reconnection rate.

At this point we mention that the energy balance is reflected in Poynting's theorem. Using equations (16), (17) and (20), and with  $\mathbf{F}_L \equiv \mathbf{J} \times \mathbf{B}$  being the Lorentz force, Poynting's theorem reads

$$P_{z=0} = \frac{\partial}{\partial t} E_{\text{mag}} + O_{\text{heat}}^{\text{dom}} + \int_0^{2l_{\text{src}}} \int_0^{4l_{\text{src}}} \mathbf{u} \cdot \mathbf{F}_L \, dx \, dz. \quad (22)$$

When the Poynting flux is negative the magnetic energy drops; it drops more quickly as the Poynting flux becomes more negative. Some of the magnetic energy is converted into heat through Ohmic heating, with the peak heating rate occurring slightly after the maximum reconnection rate. Work done on the field lines is reflected in a positive Lorentz force term in equation (22). Maximum work done coincides with the reconnection rate being maximum.

In all our experiments, the Poynting flux eventually becomes positive, indicating that from then on the sources are forced together. In

*DF* and *NoDF*, the Poynting flux becomes positive at  $t \approx 150$  and  $t \approx 200$ , respectively. This change in sign occurs when the sources have been driven far enough towards each other that the positive part of the  $B_x$  component (located outside the strength maxima of the inner sources) dominates over the negative part (located between the strength maxima). Since the horizontal velocity driver is fixed in position and time, the positive part of the  $B_x$  component can indeed become dominant if it has been brought in far enough. Flux with negative  $B_x$  is removed faster in the presence of downflows than in the absence of downflows, which explains the earlier sign change in *DF*. As a consequence of the positive Poynting flux, the magnetic energy increases. In *DF* the sign change in Poynting flux and the increase in magnetic energy happen at the same time, but in *NoDF* the magnetic energy increases only later. Heating is still strong in *NoDF* when the Poynting flux becomes positive – hence the later increase in magnetic energy in this case. The increase in magnetic energy comes from the increase of the horizontal field component. In both *DF* and *NoDF*, the maximum Poynting flux is at about time  $t = 300$ . It then develops in the same way in both cases; that is, it decreases and tends to zero.

Over time the downflow becomes gradually narrower, and changes from a double-peak flow as in Figs 6 ( $t = 65$ ) and 7 ( $t = 125$ ) to a single-peak flow at about  $t = 200$ . Figs 6 to 9 (bottom right panels) show that the amplitude in the downflow is larger in the single-peak flow than in the double-peak flow; the maximum downflow speed of about 0.056 (corresponding to about  $78 \text{ km s}^{-1}$ ) is reached at about  $t = 270$ . Eventually the downflow in *DF* ceases at about  $t = 400$ . At this time, the two experiments *DF* and *NoDF* become increasingly similar, with virtually the same Poynting flux and magnetic energy. At  $t \approx 375$ , about 10 per cent of the magnetic flux of the inner sources is left. By this time, the height of the X-point has dropped to the base. From then on, there is still some very slow reconnection and heating occurring in the domain, but reconnection is mainly happening at and very close to the base. After roughly twice the elapsed time, almost all of the remaining 10 per cent of the flux has cancelled such that less than 1 per cent is left. Furthermore, the magnetic energy has almost settled to a constant value, which is about 90 per cent of the initial magnetic energy. In both cases, however, independent of whether there are transient downflows or not, the time for complete cancellation (far below 1 per cent magnetic flux left) is  $t_{\text{cancel}} > 1000$ , corresponding to  $> 1 \text{ h}$ , if  $u_{\text{driver}} = 0.01$ .

We also drive the system at half the speed, in order to find out how our CMF event depends on the driving speed (see Fig. 5). If the driving speed is halved from  $u_{\text{driver}} = 0.01$  to  $u_{\text{driver}} = 0.005$ , we find that the time for total cancellation is twice as long, i.e.  $t_{\text{cancel}} \approx 2000$ , corresponding to approximately 2 h.

It is noticeable that, in the *NoDF* case, the brightenings resulting from Ohmic heating occur later, compared with the *DF* case, and they are longer-lived. Moreover, the XBPs in *NoDF* will be somewhat 'brighter' than the ones in *DF*, in terms of maximum heating. The total heat released is about 1.5 to 2 times larger in *NoDF* than in *DF*. Driving the system at half the speed decreases the total heat produced, but, again, the XBPs in *NoDF1/2* are about 1.5 to 2 times 'brighter' than the ones in *DF1/2*, in terms of total heat. This shows that, although the time and duration of heating are directly linked to the occurrence of reconnection, the rate of heat release and the total amount of heat are determined by the electric currents induced, for instance by the strength of flux compression. Stronger flux compression leads to higher currents and therefore to more heating. Maximum heat release by Ohmic heating and maximum reconnection rate do not have to occur at the same

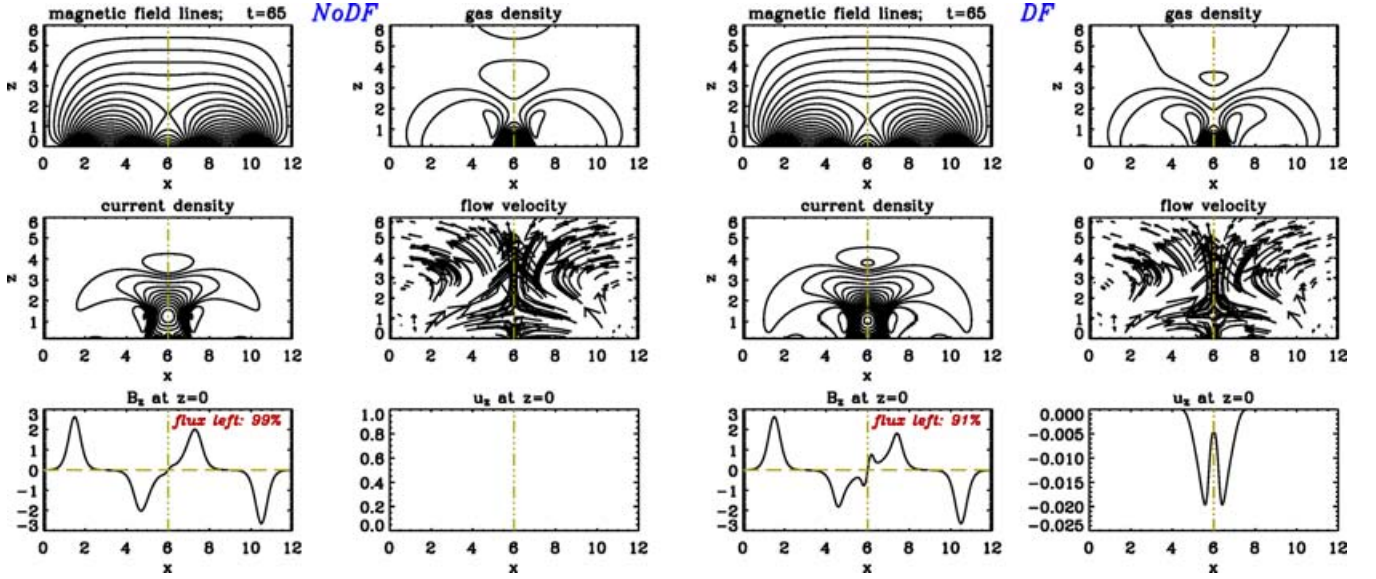


**Figure 6.** Magnetic field configuration, plasma and current densities, and flow structure, together with the vertical field and velocity at the base. Quantities are plotted at time  $t = 65$ , with downflow prohibited (left) and downflow allowed (right). The percentage values given in the bottom left panels are the remaining flux in the (moving) inner sources at the base, which is still to be cancelled. It can be seen that magnetic flux is cancelled more rapidly in *DF*.

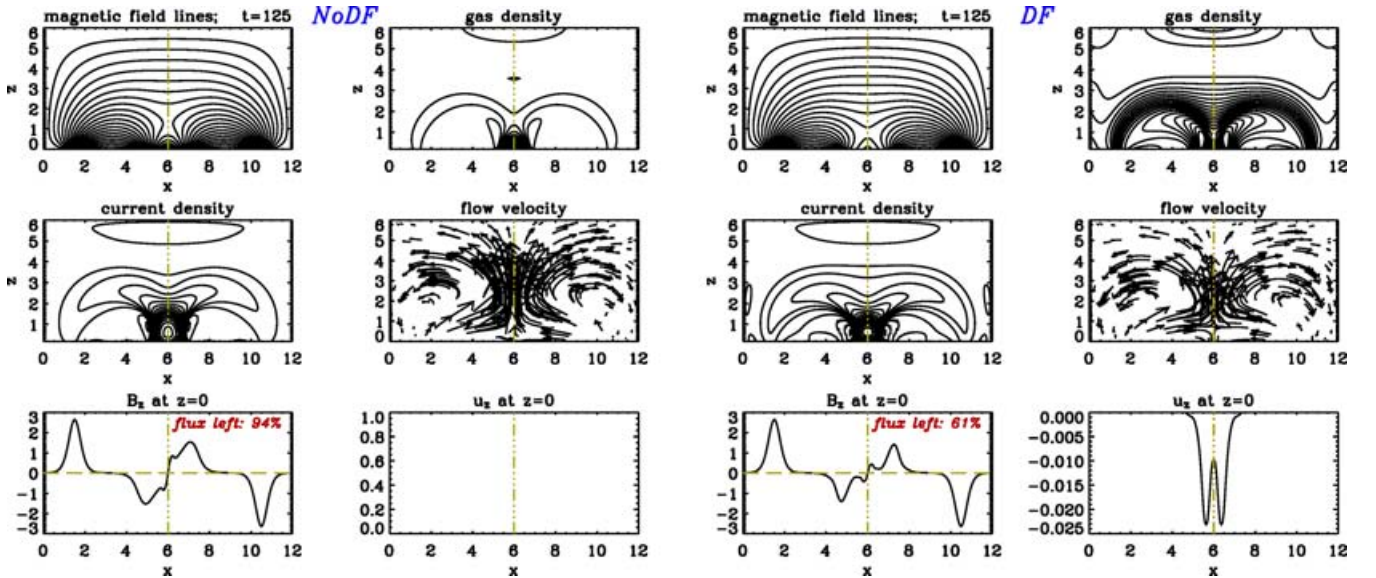


**Figure 7.** As Fig. 6, but at time  $t = 125$ .

time; in our experiments the maximum heating rate is always after the peak in the reconnection rate, in particular in the no-downflow cases.

The fact that higher currents imply more heating in our models can be understood from the following. According to Priest, Longcope & Heyvaerts (2005), the energy released during a reconnection process,  $\Delta W$ , is

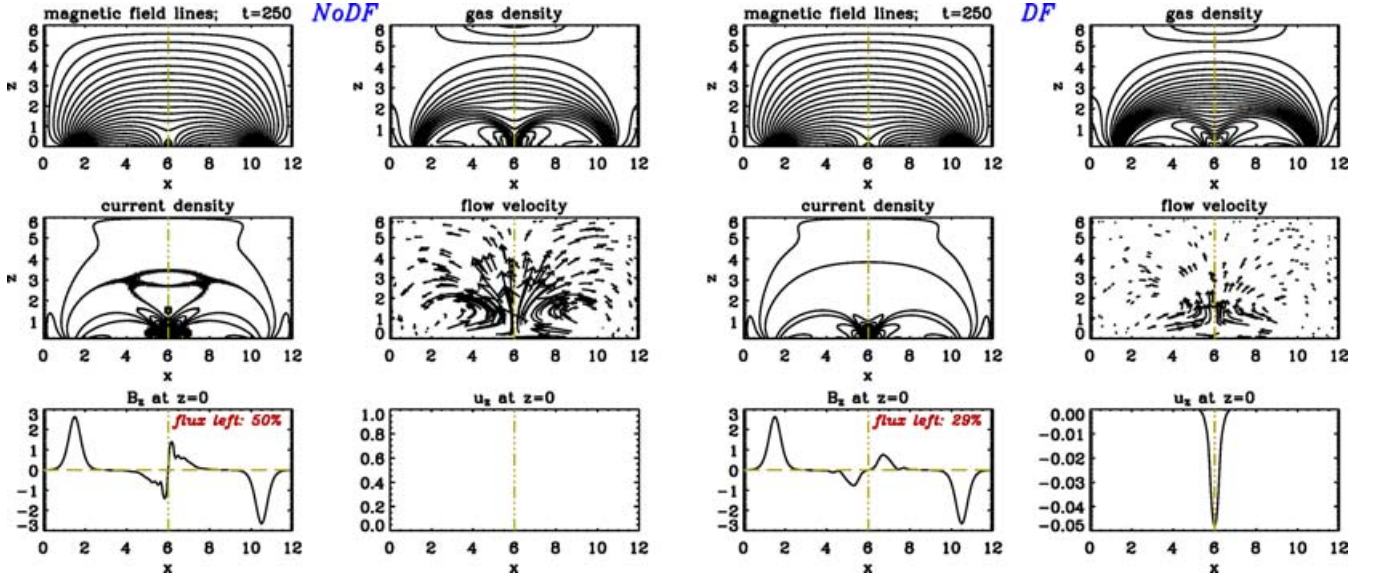
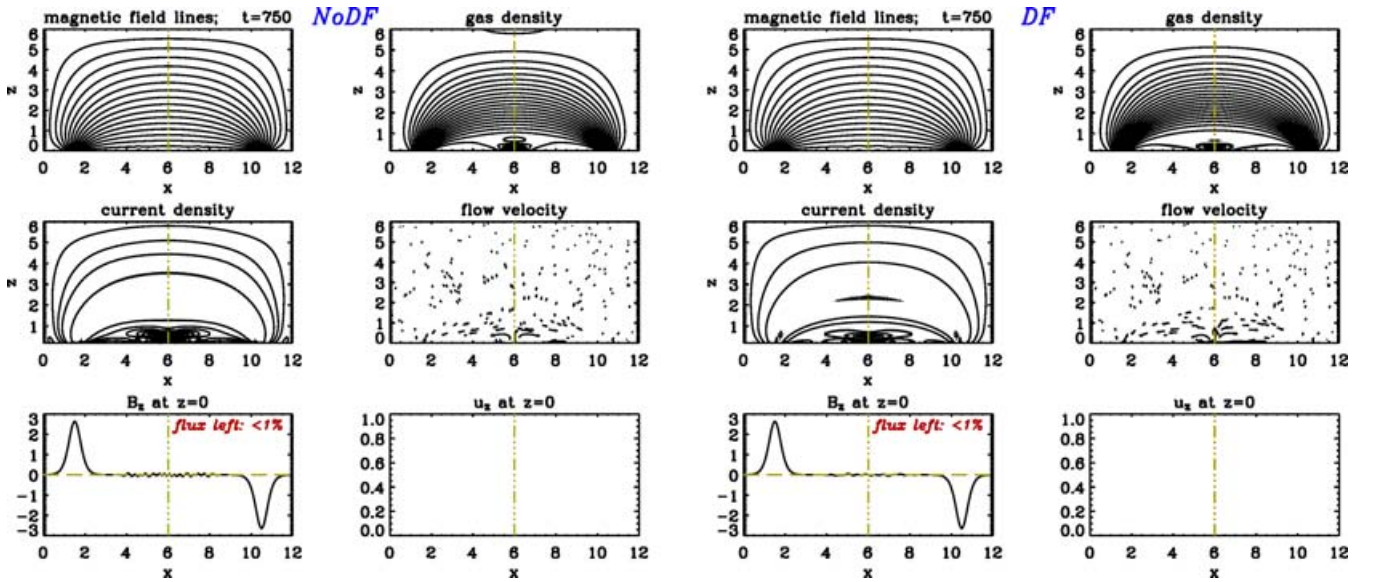
$$\Delta W \propto I \Delta \Psi, \quad (23)$$

where  $\Delta \Psi$  is the change in total flux and  $I$  is the total current. In our models, the total  $\Delta \Psi$  (i.e. the flux change occurring between the initial state and the final state) is the same in both the downflow and no-downflow cases. However, as a result of the compression in the *NoDF* case we have  $I_{NoDF} > I_{DF}$ , implying that  $(\Delta W)_{NoDF} > (\Delta W)_{DF}$ ; that is, there is a larger heat output in *NoDF*.

#### 4.4 Plasma and current densities and plasma flow

Figs 6 to 9 show, apart from the field lines in the top left panels, plasma and current densities, the plasma flow, and the vertical field strength and downflow at the base.

Not surprisingly, the largest current sheets form around the X-point, especially around the axis, but also along the upper and lower separatrices (middle left panels). This is in agreement with Rickard & Priest (1994). The plasma density is also enhanced along these separatrices (top right panels). The plasma flow initially shows a shear flow across the upper separatrices, which then turns into an aligned flow along them (middle right panels). As the X-point and so the current sheets drop in height, the flow becomes concentrated around the axis, and the density contours become aligned with the magnetic field.

Figure 8. As Fig. 6, but at time  $t = 250$ .Figure 9. As Fig. 6, but at time  $t = 750$ .

The downflow develops from a double-peak flow to a single-peak flow. Its maximum speed reaches about 0.056, corresponding to about  $78 \text{ km s}^{-1}$ . The maximum plasma velocity in the domain (except the boundary) is of the order of a few tens of kilometres per second.

## 5 CONCLUSIONS AND FUTURE WORK

We have modelled a CMF and the related formation of a coronal XBP, where cancellation is associated with flux convergence and flux submergence, and we have studied this event both in the absence and in the presence of downflows. We start off with a system of four sources of alternating polarity, but equal magnitude of flux and the same flux distribution. The inner two sources, which initially are

partially connected such that they are marginally touching at the base, are driven together until they fully cancel.

When driving the system at a maximum speed that is 0.01 or 0.005 times our characteristic Alfvén speed at the base (i.e. at a maximum speed of about 14 or  $7 \text{ km s}^{-1}$ , respectively), we find that a significant amount of thermal energy is released in the first half of the cancellation phase, during which about 90 per cent of the magnetic flux of the driven bipole is cancelled. The energy release in this phase is caused by coronal magnetic reconnection and subsequent Ohmic heating. The released energy had mainly been stored in the magnetic field, although, at later times, energy is injected into the system by a positive Poynting flux across the base. Even at those later times with positive Poynting flux, magnetic energy still continues to drop in the case for which there is significant heating still occurring. The total heat produced is of the order of  $10^{26} \text{ erg}$ ; this heat output should be

considered as a lower limit because we have not modelled a complete XBP as we start with partially connected sources. Maximum heating rates from our simulations compare well with minimum observed ones.

We have modelled a full CMF event and achieved total cancellation ( $\ll 1$  per cent flux left) after  $> 1 (> 2)$  h, when driving the system at a maximum speed of 0.01 (0.005). This lies within the wide observed range of cancellation times of 1 to 24 h (Martin, Livi & Wang 1985). The major part of magnetic flux cancellation (90 per cent) occurs during the BP phase and is associated with coronal reconnection. In the early phase, the coronal reconnection (and therefore the flux cancellation) is faster when downflows are allowed. However, the total flux cancelled during the BP phase is roughly the same in both the downflow and no-downflow cases (90 per cent). At the end of the BP phase the downflows have almost vanished, and both cases have become virtually the same. The last 10 per cent of flux is cancelled very slowly and is associated with reconnection at the base.

By comparing the magnetic field developed in the no-downflow experiments, *NoDF* and *NoDF1/2*, with the minimum energy field (the potential field; cf. *Pot*), we find that virtually no free magnetic energy is created, meaning that magnetic energy is efficiently converted to thermal energy as a result of Ohmic heating. Our driving speed of 0.0035 (0.00175) times the initial maximum Alfvén speed is slow enough for both the inertial and pressure gradient terms to remain small compared with the Lorentz force. The resulting magnetic field configurations are close to potential.

Reconnection is driven by the footpoint motions. In order to determine whether we have fast or slow reconnection, we compare our reconnection rates with the Sweet–Parker reconnection rate (Sweet 1958; Parker 1958). The Sweet–Parker reconnection rate is (see e.g. Priest & Forbes 2000)  $\mathcal{R}_{\text{mag}}^{-1/2}$ , where  $\mathcal{R}_{\text{mag}} = L \bar{v}_A / \bar{\eta}$  is the magnetic Reynolds number based on half the length of the current sheet ( $L$ ), a mean magnetic diffusivity in the current sheet ( $\bar{\eta}$ ), and a mean Alfvén speed outside the current sheet ( $\bar{v}_A$ ). Typically, we have in our simulations  $2L \approx 1.5$ ,  $\bar{\eta} \approx 0.05$ , and  $\bar{v}_A \approx 0.5$ , which gives a mean Sweet–Parker reconnection rate of  $\mathcal{R}_{\text{mag}}^{-1/2} = \sqrt{\bar{\eta}/(L \bar{v}_A)} \approx 0.365$ . A dimensionless reconnection rate from our simulations is  $R_{\text{reco}}/(L \bar{v}_A^2 \sqrt{\bar{\rho}})$ , where  $\bar{\rho} \approx 1$  is a mean plasma density outside the current sheet. Taking  $R_{\text{reco}} \leq 0.013$  from Fig. 5, this gives a reconnection rate of  $\leq 0.07$ , which is roughly 20 per cent of the mean Sweet–Parker rate estimated above, suggesting that we have slow reconnection in our experiments.

Naturally, the more rapid the driver, the faster the reconnection rate in our experiments. However, a more rapid driver also leads to shorter-lived brightenings. This is because currents are dissipated more rapidly. In the case of no downflows, there is strong flux compression, resulting in larger currents and greater mass density build-up, leading to an enhanced thermal energy release and therefore brighter XBPs. A downflow leads to more rapid flux removal and a faster reconnection rate, and, hence, to a shorter-lived XBP.

Let us now compare our numerically obtained heating rates with the analytical computations of Aly & Amari (1997). These authors consider a two-dimensional magnetic field that evolves through a sequence of quasi-potential singular equilibria. In their model, at each time-step a vertical current sheet forms, and then their magnetic field relaxes to a new potential equilibrium so that the current sheet is destroyed by some reconnection process, which is not studied in detail. Their initial X-topology is similar to ours, and the quasi-static evolution of the magnetic field is driven by ideal convergent footpoint motions (also similar to ours) pushing a magnetic bipole

together. We compare their heating rates with those obtained in our experiment *NoDF*.

Aly & Amari (1997) apply their resulting scaling law for the heating rate to an active region, where they assume a current-sheet length of 10 Mm, a typical magnetic field strength of 500 G, and a typical driving velocity of  $1 \text{ km s}^{-1}$ . They estimate an evolution time  $t_{\text{evolut}}$  of about  $10^4$  s. Their resulting heating rate is about  $0.6 \times 10^5 \text{ erg cm}^{-2} \text{ s}^{-1}$  if the diffusion time  $t_{\text{diffus}}$  satisfies  $t_{\text{diffus}} = 0.1 t_{\text{evolut}}$ , and it is about  $10^6 \text{ erg cm}^{-2} \text{ s}^{-1}$  if  $t_{\text{diffus}} = t_{\text{evolut}}$ . In order to compare these heating rates with ours, their scaling law needs to be applied to the quiet Sun. In our simulations, we have a typical current-sheet length of  $2Ll_0 \approx 1.5 l_0 \approx 7.5 \text{ Mm}$  (see above), a maximum magnetic field strength of  $B_{\text{src}} \approx 2.83 B_0 \approx 14 \text{ G}$ , and in experiment *NoDF* a maximum coronal base driving velocity of  $u_{\text{driver}} v_0 = 0.01 v_0 \approx 14 \text{ km s}^{-1}$ . (Note that if we take into account that our base is located in the low corona, above the photosphere, our maximum *photospheric* driving velocity would be approximately  $u_{\text{driver}}^{\text{photo}} v_0 \approx u_{\text{driver}} v_0 \sqrt{B_{\text{src}}/B_{\text{src}}^{\text{photo}}} \approx 1.7 \text{ km s}^{-1}$ , if we assumed a maximum photospheric magnetic field strength of  $B_{\text{src}}^{\text{photo}} \approx 1000 \text{ G}$ ; cf. Mandrini, Démoulin & Klimchuk 2000.)

The heating rate of Aly & Amari (1997) scales with the field strength squared and with the driving velocity squared. Thus, applying their model to a region of the quiet Sun as considered by us, they would find a heating rate of  $0.9 \times 10^4 \text{ erg cm}^{-2} \text{ s}^{-1}$  if  $t_{\text{diffus}} = 0.1 t_{\text{evolut}}$  and of  $1.5 \times 10^5 \text{ erg cm}^{-2} \text{ s}^{-1}$  if  $t_{\text{diffus}} = t_{\text{evolut}}$ . Our evolution time for the heating event in experiment *NoDF* and our diffusion time are  $t_{\text{evolut}} \approx 400 t_0 \approx 1440 \text{ s}$  and  $t_{\text{diffus}} \equiv t_0 (2L)^2 / \bar{\eta} \approx 45 t_0 \approx 162 \text{ s}$ , respectively, so that we have  $t_{\text{diffus}} \approx 0.1 t_{\text{evolut}}$ . Our heating rate of about  $1.5 \times 10^4 \text{ erg cm}^{-2} \text{ s}^{-1}$  (see Section 4.2) therefore is very similar to that of Aly & Amari (1997).

How do our heating rates scale with the driving velocity ( $v$ )? Different coronal heating models predict different scaling laws for the heating rate with  $v$  (Mandrini et al. 2000). The reconnection models of Parker (1983) predict a scaling as  $v^2$  or  $v^{1.5}$  and, as already mentioned above, the current-sheet model by Aly & Amari (1997) predicts a scaling as  $v^2$ . In *NoDF*, we have a maximum heating rate of 0.000675 in the domain and of 0.00075 at the axis (cf. Fig. 5). In the experiment with half the driving speed, *NoDF1/2*, the corresponding heating rates are 0.0003 and 0.000325, respectively. Thus, we find that scaling is as  $v^f$  with  $f \approx 1.2$ .

Work is in progress on new experiments, in which we start the simulations with a totally unconnected inner bipole in order to model a complete XBP. We also have begun considering magnetic fragments with unequal sources, because in general observed CMFs involve unequal sources. More realistic modelling would include gravity and a stratified, non-isothermal lower atmosphere. Furthermore, two-dimensional simulations should be compared in the future with three-dimensional simulations (extending previous work by Dreher, Birk & Neukirch 1997 and Büchner, Nikutowski & Otto 2004) in order to see what features survive and what new features arise by including the third dimension. Moreover, in a three-dimensional model it would be possible to study CMFs that involve more than one magnetic bipole.

## ACKNOWLEDGMENTS

Use of the supercomputer SGI 3800 in Linköping and of the PPARC-supported supercomputer in St Andrews is acknowledged, together with financial support from PPARC on the St Andrews Solar Rolling Grant.

**REFERENCES**

- Aly J. J., Amari T., 1997, *A&A*, 319, 699  
 Beveridge C., Priest E. R., Brown D. S., 2002, *Solar Physics*, 209, 333  
 Büchner J., Nikutowski B., Otto A., 2004, in Ireland J., Walsh R. W., eds, *ESA SP-575, Proc. SOHO Workshop 15, Coronal Heating*. ESA, Noordwijk, p. 23  
 Chae J., Moon Y.-J., Pevtsov A. A., 2004, *ApJ*, 602, L65  
 Close R. M., Parnell C. E., Longcope D. W., Priest E. R., 2004, *ApJ*, 612, L81  
 Dreher J., Birk G. T., Neukirch T., 1997, *A&A*, 323, 593  
 Golub L., Krieger A. S., Silk J. K., Timothy A. F., Vaiana G. S., 1974, *ApJ*, 189, L93  
 Golub L., Krieger A. S., Vaiana G. S., 1976, *Solar Physics*, 49, 79  
 Golub L., Krieger A. S., Harvey J. W., Vaiana G. S., 1977, *Solar Physics*, 53, 111  
 Habbal S. R., Withbroe G. L., 1981, *Solar Physics*, 69, 77  
 Hagenaar H. J., 2001, *ApJ*, 555, 448  
 Harvey K. L., 1985, *Aust. J. Phys.*, 38, 875  
 Harvey K. L., 1996, in Bentley R. D., Mariska J. T., eds, *ASP Conf. Ser. Vol. 111, Magnetic Reconnection in the Solar Atmosphere*. Astron. Soc. Pac., San Francisco, p. 9  
 Harvey K. L., Jones H. P., Schrijver C. J., Penn M. J., 1999, *Solar Physics*, 190, 35  
 Livi S. H. B., Wang J., Martin S. F., 1985, *Aust. J. Phys.*, 38, 855  
 Longcope D. W., 1998, *ApJ*, 507, 433  
 Longcope D. W., Kankelborg C. C., 1999, *ApJ*, 524, 483  
 Longcope D. W., Kankelborg C. C., Nelson J. L., Pevtsov A. A., 2001, *ApJ*, 553, 429  
 Mackay D. H., Galsgaard K., Priest E. R., Foley C. R., 2000, *Solar Physics*, 193, 93  
 Mandrini C. H., Démoulin P., Van Driel-Gesztelyi L., Schmieder B., Cauzzi G., Hofmann A., 1996, *Solar Physics*, 168, 115  
 Mandrini C. H., Démoulin P., Klimchuk J. A., 2000, *ApJ*, 530, 999  
 Martin S. F., Livi S. H. B., Wang J., 1985, *Aust. J. Phys.*, 38, 929  
 Parker E. N., 1958, *ApJ*, 128, 664  
 Parker E. N., 1983, *ApJ*, 264, 642  
 Parnell C. E., Galsgaard K., 2004, *A&A*, 428, 595  
 Parnell C. E., Jupp P. E., 2000, *ApJ*, 529, 554  
 Parnell C. E., Priest E. R., 1995, *Geophys. Astrophys. Fluid Dyn.*, 80, 255  
 Parnell C. E., Priest E. R., Golub L., 1994a, *Solar Physics*, 151, 57  
 Parnell C. E., Priest E. R., Titov V. S., 1994b, *Solar Physics*, 153, 217  
 Priest E. R., Forbes T. G., 2000, *Magnetic Reconnection: MHD Theory and Applications*. Cambridge Univ. Press, Cambridge.  
 Priest E. R., Parnell C. E., Martin S. F., 1994, *ApJ*, 427, 459  
 Priest E. R., Longcope D. W., Heyvaerts J., 2005, *ApJ*, 624, 1057  
 Rickard G. J., Priest E. R., 1994, *Solar Physics*, 151, 107  
 Sweet P. A., 1958, *Nuovo Cimento*, 8, 188  
 Webb D. F., Martin S. F., Moses D., Harvey J. W., 1993, *Solar Physics*, 144, 15  
 Withbroe G. L., Noyes R. W., 1977, *ARA&A*, 15, 363

This paper has been typeset from a  $\text{\TeX}/\text{\LaTeX}$  file prepared by the author.